

A LOG-GAUSSIAN COX PROCESS WITH SEQUENTIAL MONTE CARLO FOR LINE NARROWING IN SPECTROSCOPY

TEEMU HÄRKÖNEN*, EMMA HANNULA

School of Engineering Science
LUT University
Yliopistonkatu 34, FI-53850 Lappeenranta, Finland

MATTHEW T. MOORES

National Institute for Applied Statistics Research Australia
University of Wollongong
Wollongong NSW 2522, Australia

ERIK M. VARTIAINEN, LASSI ROININEN

School of Engineering Science
LUT University
Yliopistonkatu 34, FI-53850 Lappeenranta, Finland

(Communicated by the associate editor name)

ABSTRACT. We propose a statistical model for narrowing line shapes in spectroscopy that are well approximated as linear combinations of Lorentzian or Voigt functions. We introduce a log-Gaussian Cox process to represent the peak locations thereby providing uncertainty quantification for the line narrowing. Bayesian formulation of the method allows for robust and explicit inclusion of prior information as probability distributions for parameters of the model. Estimation of the signal and its parameters is performed using a sequential Monte Carlo algorithm followed by an optimization step to determine the peak locations. Our method is validated using a simulation study and applied to a mineralogical Raman spectrum.

1. Introduction. In signal processing, it is often fruitful to analyze a time series through its spectral density representation, or periodogram [1]. The frequencies or wavenumbers contained in the observed signal are displayed along the horizontal axis, while the corresponding energy intensities are displayed on the vertical axis. In many cases, the spectrum exhibits peaks with a certain line shape, which can be characterized by a spectral density function. Examples include ocean waves [32], ionospheric spectra measured by incoherent scatter radar [36], and X-ray spectra used for industrial quality control [33]. In this paper we focus on the specific example of Raman spectroscopy [31], but the methods that we discuss are much more broadly applicable to many other kinds of spectra.

Line narrowing of spectral line shapes is a mathematical procedure that is used to improve the resolution of spectroscopy. The principal aim of line narrowing is

2020 *Mathematics Subject Classification.* Primary: 62F15, 62L12; Secondary: 78M31.

Key words and phrases. Bayesian inference, Fourier self-deconvolution, particle filtering and smoothing, Poisson process, peak detection, statistical signal processing.

* Corresponding author: Teemu Härkönen.

to reduce overlap of the line shapes and to infer more accurate information on the line shape position. There is a long history of research in various approaches for line narrowing based on ideas such as Fourier self-deconvolution [14, 16, 17], Tikhonov regularization [4, 21], maximum entropy [2, 22], and Bayesian inference [11, 12, 27]. Nevertheless, the applicability of these algorithms tends to be limited by requirements on input parameters not known in general, meaning that they must be hand-tuned, and also by the signal-to-noise ratio of the measurements.

To consider a specific example of line-narrowing algorithm, Line-shape Optimized Maximum Entropy linear Prediction (LOMEP) works well only for spectra with a limited number of spectral lines, which all have the same *a priori* known line shape [14]. Nevertheless, the fundamental idea behind LOMEP is very appealing. It uses a technique called Fourier self-deconvolution [16, 17], where the Fourier transform of the data is divided by the Fourier transform of a parameterized kernel function, resulting in a signal with narrower line shapes. This requires *a priori* knowledge of the line-shape function in the original spectrum. A low-pass filter is applied to the obtained non-decaying signal to ensure high signal-to-noise ratio. After this, a maximum-entropy, linear-prediction algorithm is used to predict the non-decaying signal to yield new narrower line shapes while preserving their respective amplitudes.

In our previous work [13], we incorporated LOMEP as a pre-processing step for empirical Bayesian inference on the line shape parameters using a Sequential Monte Carlo (SMC) algorithm [6]. Here, we extend this approach to a fully-Bayesian statistical model that is capable of providing posterior distributions for the estimated line-narrowed spectrum, along with posterior distributions for the line width and impulse-response length. We sample these model parameters and realizations using SMC, which utilizes a collection of particles to approximate the probability distributions of interest. Our SMC algorithm provides a scalable and parallelizable method of statistical inference for spectroscopic data.

The LOMEP algorithm is known to suffer from peak splitting, where individual peaks in the underlying signal are split into two or more peaks, thereby overestimating the number of peaks that are present [15]. The key contribution of this paper is the introduction of a Log-Gaussian Cox Process (LGCP) [25] for this specific application, as a statistical model for the peak locations. An LGCP is a doubly-stochastic process, whose output is defined as a Poisson process and whose intensity function is modelled as a log-Gaussian process. This enables modelling of observed point data that exhibit clustering, the intensity of which can vary spatially or temporally. The LGCP has previously been applied to statistical modelling of disease incidence data [9], wildfire occurrences [29], and crime incidence [30]. Here, the intensity function of the LGCP can be considered to provide automatic smoothing where the parameters of the smoothing kernel are inferred statistically. For the LGCP intensity function, we use a maximum *a posteriori* (MAP) estimate. In addition to the primary interest of line narrowing, the posterior distributions for the line widths and peak locations have immediate applications in being incorporated as prior distributions for further statistical spectrum analysis techniques [13, 24].

The remainder of this paper is structured as follows. In Section 2, we present our Bayesian statistical model for spectral measurements. In Section 3, this is followed by a description of the SMC algorithm. In Section 4, we formulate our log-Gaussian Cox process model to better estimate the underlying line-narrowed spectrum. In Section 5, we present our results for a simulation-based calibration study [34, 23]. In Section 6, prior distributions and other modelling choices are detailed. In Section

7, we present experimental results for our synthetic and real spectroscopic data sets. Finally, in Section 8, we discuss our conclusions and consider future directions for research.

2. Statistical line narrowing model. We observe K spectral measurements consisting of N line shapes with additive errors

$$y_k = y(\nu_k) = f(\nu_k; \delta_N(\nu_k; \mathbf{a}, \mathbf{l}), \boldsymbol{\theta}) + \epsilon_k, \quad (1)$$

where $y_k \in \mathbb{R}$ denotes a discretized measurement at a wavenumber location $\nu_k \in \{\nu_1, \dots, \nu_K\}$ in the space of wavenumbers $\mathcal{S} \subset \mathbb{R}_+$. Wavenumbers are measured in inverse centimetres (cm^{-1}), while the units of the intensities are application-dependent. In this paper, y_k is measured in scientific arbitrary units (a.u.). The space \mathcal{S} has been discretized with sampling resolution $h > 0$ where $h = |\nu_{k+1} - \nu_k|$. We denote the vector of all measurements as $\mathbf{y} := (y_1, \dots, y_K)^T$. The continuous spectral density model $f(\cdot)$ and its parameters $\mathbf{a}, \mathbf{l}, \boldsymbol{\theta}$ are described in detail below. The Gaussian measurement error is $\epsilon_k \sim \mathcal{N}(0, \sigma_\epsilon^2)$ with variance assumed known and zero mean.

The spectral density model is given by

$$f(\nu; \delta_N(\nu; \mathbf{a}, \mathbf{l}), \boldsymbol{\theta}) = \sum_{n=1}^N a_n \mathcal{K}_\bullet(\nu - l_n; \boldsymbol{\theta}) = \mathcal{K}_\bullet(\nu; \boldsymbol{\theta}) * \delta_N(\nu; \mathbf{a}, \mathbf{l}), \quad (2)$$

where $*$ denotes convolution with respect to ν and

$$\delta_N(\nu; \mathbf{a}, \mathbf{l}) := \sum_{n=1}^N a_n \delta(\nu - l_n), \quad (3)$$

which is a linear combination of N Dirac delta functions $\delta(\nu)$ at locations $\mathbf{l} = (l_1, \dots, l_N)^T$, with amplitudes $\mathbf{a} = (a_1, \dots, a_N)^T$.

The common line shape, or kernel, $\mathcal{K}_\bullet(\nu; \boldsymbol{\theta})$ is parameterized according to a vector of P line shape parameters, $\boldsymbol{\theta} = (\theta_1, \dots, \theta_P)^T$. We consider two common line shapes relevant for spectroscopic applications, the Lorentz line shape

$$\mathcal{K}_L(\nu; \gamma) = \frac{1}{\pi\gamma} \frac{\gamma^2}{\nu^2 + \gamma^2}, \quad (4)$$

with $P = 1$ scale parameter $\theta_1 \equiv \gamma$, and the Voigt line shape

$$\mathcal{K}_V(\nu; \sigma, \gamma) = \mathcal{K}_L(\nu; \gamma) * \mathcal{K}_G(\nu; \sigma) = \frac{1}{\pi\gamma} \frac{\gamma^2}{\nu^2 + \gamma^2} * \frac{1}{\sqrt{2\pi}\sigma^2} \exp\left(-\frac{\nu^2}{2\sigma^2}\right), \quad (5)$$

with $P = 2$ parameters, $\theta_1 \equiv \gamma$ and $\theta_2 \equiv \sigma$, which denote the scale parameters of Lorentzian and Gaussian line shapes, respectively. In Raman spectroscopy, the Lorentzian line shape results from collisional broadening between molecules, while the Gaussian line shape results from Doppler broadening. When both of these mechanisms are active simultaneously, this results in a Voigt line shape [8]. Illustrations of Lorentzian line shapes and the corresponding Dirac delta functions are shown in Figure 1.

The preceding construction gives a generative model for data y_k , where the parameters are known. In order to learn the parameters from observed data, a different but related perspective is needed. In the Fourier domain, the Dirac delta functions

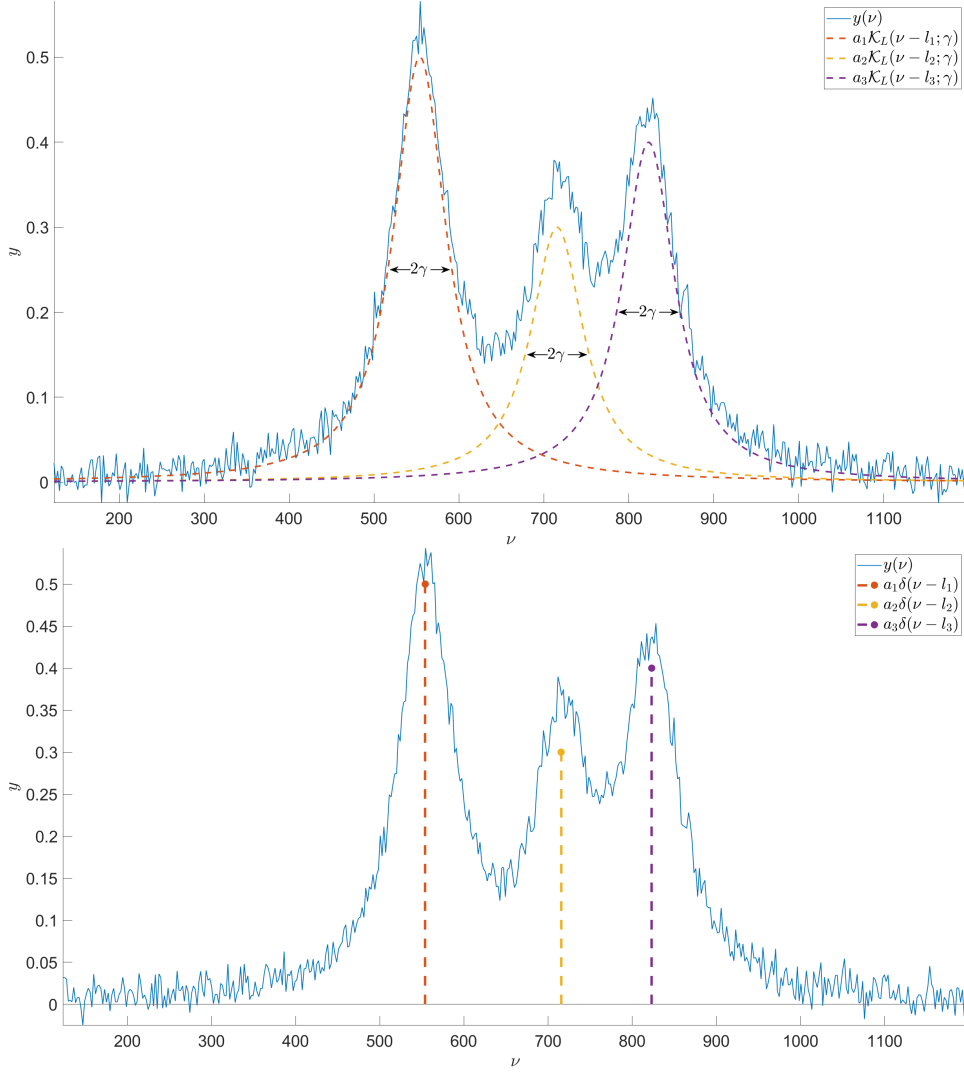


FIGURE 1. On top, a spectrum (blue) consisting of $N = 3$ Lorentzian line shapes located at locations $(l_1, l_2, l_3)^T$ shown in red, yellow, and purple, respectively. Upon successful line narrowing, or deconvolution, we would obtain three individual Dirac delta functions located at $(l_1, l_2, l_3)^T$. The aim of this paper is to construct approximate samples for the Dirac delta functions using linear prediction which are further modelled as a log-Gaussian Cox process.

can be represented in terms of the Fourier self-deconvolution signal [16]

$$\begin{aligned} \xi(\omega; \mathbf{a}, \mathbf{l}, \boldsymbol{\theta}) &:= \mathcal{F} \left\{ \sum_{n=1}^N a_n \delta(\nu - l_n) + a_n \delta(\nu + l_n) \right\} = 2 \sum_{n=1}^N a_n \cos(2\pi \omega l_n) \\ &\approx \frac{\mathcal{F} \{y(\nu) + y(-\nu)\}}{\mathcal{F} \{\mathcal{K}_{\bullet}(\nu; \boldsymbol{\theta})\}}, \end{aligned} \quad (6)$$

where \mathcal{F} is the Fourier transform and ω denotes the Fourier-transformed variable. Convolution in $\nu \in \mathcal{S}$ corresponds to multiplication in the Fourier domain, $\omega \in \Omega$ [17]. Therefore, when we divide by $\mathcal{F}\{\mathcal{K}_\bullet(\nu; \boldsymbol{\theta})\}$ in Equation (6), this operation corresponds to deconvolution. The continuous Fourier transform of the Dirac delta function is equal to the cosine function. In practice, the domain \mathcal{S} has been discretized, so we employ the discrete Fourier transform (DFT). We first reflect the observation vector \mathbf{y} about the origin to obtain $y(+\nu_k)$ and $y(-\nu_k)$ for $k = 1, \dots, K$ to produce an even function. This is so that the DFT results in a real-valued Fourier representation. However, the presence of noise in \mathbf{y} means that the deconvolution is only approximate. This approximation error balloons as the Fourier transform of the kernel $\mathcal{K}_\bullet(\nu; \boldsymbol{\theta})$ in the denominator of Equation (6) approaches zero.

The aforementioned approximations result in only part of the discrete Fourier self-deconvolution signal being useful. This useful part is truncated from the full-length signal to length $2 \leq M \leq K$ first samples. The M samples are then used to linearly predict the signal to the original length, K . The linear prediction is performed as a recursive one-point extrapolation

$$\xi_{\text{LP}}(\omega_k; \boldsymbol{\theta}, M) = \Delta\omega \sum_{i=1}^M r_i \xi(\omega_{k-i}; \mathbf{a}, \mathbf{l}, \boldsymbol{\theta}), \quad (7)$$

for $k = M+1, \dots, K$, where $\Delta\omega$ is the equidistant spacing and r_i is the i th LOMEP impulse response coefficient. We use Levinson-Durbin recursion and Burg's formula to estimate the impulse response $\mathbf{r} = (r_1, \dots, r_M)^T$ [14, 17].

Under the assumptions given in Equation (1) the exact likelihood of the observed spectrum is

$$\mathcal{L}(\mathbf{y} \mid \mathbf{f}(\boldsymbol{\nu}; \mathbf{a}, \mathbf{l}, \boldsymbol{\theta}), \sigma_\epsilon^2) = \prod_{k=1}^K \mathcal{N}(y_k; f(\nu_k; \delta_N(\nu_k; \mathbf{a}, \mathbf{l}, \boldsymbol{\theta}), \sigma_\epsilon^2), \quad (8)$$

where $\mathbf{f}(\boldsymbol{\nu}; \mathbf{a}, \mathbf{l}, \boldsymbol{\theta}) = (f(\nu_1; \delta_N(\nu_1; \mathbf{a}, \mathbf{l}, \boldsymbol{\theta}), \sigma_\epsilon^2), \dots, f(\nu_K; \delta_N(\nu_K; \mathbf{a}, \mathbf{l}, \boldsymbol{\theta}), \sigma_\epsilon^2))^T$ is the underlying spectral signal evaluated at wavenumbers $\boldsymbol{\nu} = (\nu_1, \dots, \nu_K)^T$. However, in practice this signal is unknown and cannot be directly observed. Instead, we approximate it using

$$f(\nu_k; \delta_N(\nu_k; \mathbf{a}, \mathbf{l}, \boldsymbol{\theta})) \approx g(\nu_k, \boldsymbol{\theta}, M) := \mathcal{F}^{-1} \left\{ \xi_{\text{LP}}(\omega; \boldsymbol{\theta}, M) \mathcal{F}\{\mathcal{K}_\bullet(\nu, \boldsymbol{\theta})\} \right\}(\nu_k), \quad (9)$$

where \mathcal{F}^{-1} denotes the inverse DFT.

For brevity, henceforth we use a shorthand notation for the line-narrowed spectrum $\mathbf{x}_{\text{LN}} := (x_{\text{LN}}(\nu_1; \boldsymbol{\theta}, M), \dots, x_{\text{LN}}(\nu_K; \boldsymbol{\theta}, M))^T = \mathcal{F}^{-1} \{\xi_{\text{LP}}(\omega; \boldsymbol{\theta}, M)\}$. The likelihood (8) can then be approximated by

$$\mathcal{L}(\mathbf{y} \mid \mathbf{f}(\boldsymbol{\nu}; \mathbf{a}, \mathbf{l}, \boldsymbol{\theta}), \sigma_\epsilon^2) \approx \tilde{\mathcal{L}}(\mathbf{y} \mid \mathbf{x}_{\text{LN}}, \sigma_\epsilon^2) = \prod_{k=1}^K \mathcal{N}(y_k; g(\nu_k, \boldsymbol{\theta}, M), \sigma_\epsilon^2). \quad (10)$$

The idea of approximating the likelihood using a Fourier transform is similar in spirit to the Whittle quasi-likelihood [37], but in our case $\tilde{\mathcal{L}}$ also involves deconvolution, truncation, and linear prediction. An example of \mathbf{x}_{LN} is shown at the top of Figure 2, corresponding to the spectrum in Figure 1. The problems of peak splitting, ringing artifacts and negative values common to LOMEP are clearly evident in this figure.

Given our quasi-likelihood, the approximate posterior distribution can be formulated as

$$\pi(\mathbf{x}_{\text{LN}}, \boldsymbol{\theta}, M \mid \mathbf{y}, \sigma_\epsilon^2) \propto \tilde{\mathcal{L}}(\mathbf{y} \mid \mathbf{x}_{\text{LN}}, \sigma_\epsilon^2) \pi_0(\mathbf{x}_{\text{LN}} \mid \boldsymbol{\theta}, M) \pi_0(\boldsymbol{\theta}) \pi_0(M), \quad (11)$$

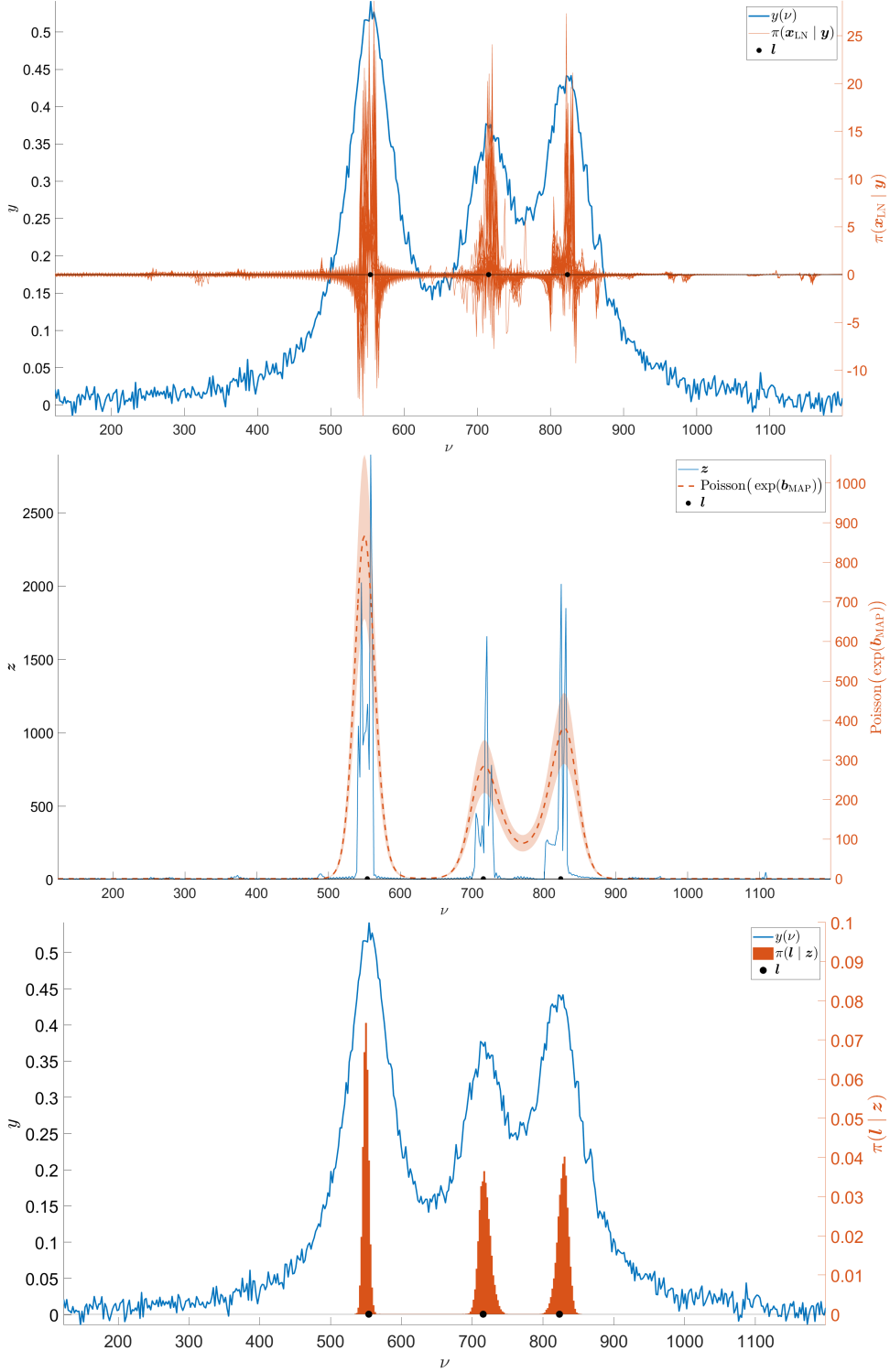


FIGURE 2. On top, a summary of the distribution of posterior samples from $\pi(x_{LN} | y)$ for the spectrum in Figure 1. In the middle, marginalized posterior samples according to Eq. (20) and the corresponding LGCP estimate. At the bottom, the posterior $\pi(l | z)$ for the line shape locations l obtained by sampling the LGCP local maxima.

where $\pi_0(\boldsymbol{\theta})$, $\pi_0(M)$, and $\pi_0(\mathbf{x}_{\text{LN}} \mid \boldsymbol{\theta}, M)$ denote prior distributions for the line width, the Fourier self-deconvolution cut-off point, and the line-narrowed spectrum, respectively. The probability distribution defined in Equation (11) is not available in closed form and thus we require Bayesian computational methods to obtain stochastic samples from this distribution. The SMC algorithm that we use for this purpose is similar to the algorithm in [13] but with different likelihood and prior distribution formulations. This is similar in spirit to methods such as SMC-ABC [7], which also targets an approximate posterior. The quasi-likelihood approximation (10) that we have introduced above substantially reduces the computational cost, as we discuss in the following section.

3. Sequential Monte Carlo. SMC, also known as the particle filter, or sequential importance sampling with resampling, is a class of algorithms for Bayesian computation that are very widely used for statistical signal processing and time series analysis. For a general overview of SMC methods, we recommend [3, 28]. The SMC algorithm that we introduce here employs sequential importance sampling from a series of tempered probability distributions $\pi^{(0)}, \pi^{(1)}, \dots, \pi^{(T)}$ to ultimately obtain samples from the desired posterior distribution defined in Equation (11).

We construct the distribution at step t of the tempering sequence as

$$\pi^{(t)}(\mathbf{x}_{\text{LN}}, \boldsymbol{\theta}, M \mid \mathbf{y}, \sigma_\epsilon^2) \propto \tilde{\mathcal{L}}(\mathbf{y} \mid \mathbf{x}_{\text{LN}}, \sigma_\epsilon^2)^{\kappa^{(t)}} \pi_0(\mathbf{x}_{\text{LN}} \mid \boldsymbol{\theta}, M) \pi_0(\boldsymbol{\theta}) \pi_0(M) \quad (12)$$

where the superscript (t) denotes the iteration of the SMC algorithm and the tempering parameter $\kappa^{(t)}$ is chosen such that $\kappa^{(t-1)} < \kappa^{(t)} < \kappa^{(t+1)} < \dots \leq 1$ with $\kappa^{(0)} = 0$. In Equation (12), the initial state of the particle distribution is equal to the joint prior for $\boldsymbol{\theta}$, M , and \mathbf{x}_{LN} : that is $\pi^{(0)} = \pi_0(\mathbf{x}_{\text{LN}} \mid \boldsymbol{\theta}, M) \pi_0(\boldsymbol{\theta}) \pi_0(M)$. At each subsequent iteration, the particles are updated so that the intermediate tempering distribution approaches the targeted posterior given in Equation (11).

We determine the tempering schedule adaptively, as in [13, 24], such that the relative decrease in effective sample size (ESS), defined as

$$J_{\text{ESS}}^{(t)} = \frac{1}{\sum_{j=1}^J \left(w_j^{(t)}\right)^2}, \quad (13)$$

is approximately some predefined learning rate η between SMC iterations. Here, $w_j^{(t)}$ is the importance sampling weight for the j th particle $(\mathbf{x}_{\text{LN},j}, \boldsymbol{\theta}_j, M_j)$, where $j = 1, \dots, J$. The incremental unnormalized weights in the SMC algorithm are

$$W_j^{(t)} \propto \frac{\tilde{\mathcal{L}}(\mathbf{y} \mid \mathbf{x}_{\text{LN}}, \sigma_\epsilon^2)^{\kappa^{(t)}}}{\tilde{\mathcal{L}}(\mathbf{y} \mid \mathbf{x}_{\text{LN}}, \sigma_\epsilon^2)^{\kappa^{(t-1)}}} w_j^{(t-1)}, \quad (14)$$

with the normalized weights given by $w_j^{(t)} = W_j^{(t)} / \sum_{j=1}^J W_j^{(t)}$.

As the number of iterations increases, the weights will gradually become concentrated on a small number of particles, hence $J_{\text{ESS}}^{(t)}$ decreases. This can eventually result in a single particle dominating the inference. To avoid this tendency, we employ two additional steps: resampling and mutation of the particles. Resampling is initiated when the ESS drops below a set threshold J_{min} . Each particle is resampled with replacement, using probabilities equal to $w_j^{(t)}$. This often means that particles with the most weight are sampled multiple times, creating duplicates. After resampling, the weights are all reset to $w_j^{(t)} = \frac{1}{J}$. Markov chain Monte Carlo (MCMC) is then used to update the particles to move duplicate particles to different states.

The target distribution for the MCMC is defined by the tempered posterior distribution at iteration t as given in Equation (12). We present pseudo-code for our SMC sampled line narrowing method in Algorithm 1. After the final iteration is

Algorithm 1 Sequential Monte Carlo sampled line narrowing.

Initialize:

Set $t = 0$ and $\kappa^{(t)} = 0$.

Sample J particles independently from the prior $\pi_0(\boldsymbol{\theta})\pi_0(M)$.

Compute a line-narrowed spectrum $\mathbf{x}_{\text{LN},j}$ for each particle $(\boldsymbol{\theta}_j, M_j)$.

Compute the quasi-likelihood $\tilde{\mathcal{L}}(\mathbf{y} \mid \mathbf{x}_{\text{LN},j}, \sigma_\epsilon^2)$ for each particle.

Set particle weights $w_j^{(t)} = \frac{1}{J}$.

while $\kappa^{(t)} < 1$ **do**

$t = t + 1$.

Determine $\kappa^{(t)}$ according to the learning rate η .

Update particle weights $w_j^{(t)}$ according to Equation (14).

Compute the effective sample size $J_{\text{ESS}}^{(t)}$ using Equation (13).

if $J_{\text{ESS}}^{(t)} < J_{\text{min}}$ **then**

Resample particles according to their weights.

Set particle weights $w_j^{(t)} = \frac{1}{J}$.

end if

Update particles with MCMC targeting the tempered posterior given by (12).

end while

complete and $\kappa^{(T)} = 1$, the distribution of the J particles represent samples from the target posterior distribution, Equation (11).

Linear prediction requires Fast Fourier transforms (FFT) of size K , which are $\mathcal{O}(K \log(K))$, solving a Toeplitz matrix at worst of size $M_{\text{max}} \times M_{\text{max}}$ where M_{max} is the upper bound defined by the prior $\pi_0(M)$ resulting in $\mathcal{O}(M_{\text{max}}^2)$, and the complexity of the prediction is at worst $K - M$ values with M impulse response coefficients which is $\mathcal{O}((K - M)M)$. For large enough K and $M_{\text{max}} \ll K$, the cost of linear prediction is dominated by the complexity of the FFT, $\mathcal{O}(K \log(K))$. The linear prediction is performed at each step t of the SMC sampling N_{MCMC} times where N_{MCMC} is the number of MCMC iterations. This leads to a total of $T N_{\text{MCMC}}$ likelihood evaluations, resulting in a total complexity of $\mathcal{O}(KT \log(K))$.

However, the marginal posterior $\pi(\mathbf{x}_{\text{LN}} \mid \mathbf{y})$ for the line-narrowed spectrum is lacking in physical interpretability. This is due to the phenomenon of “peak splitting,” where individual peaks in the true spectrum $\mathbf{f}(\boldsymbol{\nu}; \boldsymbol{\theta})$ are split into two or more peaks in the line-narrowed spectrum \mathbf{x}_{LN} [15]. The line-narrowed spectra are approximations of Dirac delta functions, so their marginalization is difficult to visualize accurately. We show a simplified illustration of the marginalized posterior for \mathbf{x}_{LN} in Figure 2. This leads us to consider “smoothing” the peaks, or more accurately, estimating the underlying distribution of peak locations l_n , which we assume to be distributed according to a log-Gaussian Cox process.

4. Log-Gaussian Cox Process. A point process is a countable collection of random locations $\{l_1, l_2, \dots\}$ within some space, \mathcal{S} . In our case, we take \mathcal{S} to be the one-dimensional space of wavenumbers \mathbb{R}_+ , or more specifically the continuous interval bounding the fingerprint region for organic molecules, $l_n \in [120, 1200]$.

Closely related to this random set of points is the counting process $\varphi(A)$ for measurable subsets $A \subseteq \mathcal{S}$. For example, if $A = [800, 900]$ and there are two peaks with locations $l_1 = 810$ and $l_2 = 850$, then $\varphi(A) = 2$.

A Poisson process is a type of point process that satisfies the following properties [19]:

- (i) Whenever $A_1, A_2, \dots, A_Q \subset \mathcal{S}$ are disjoint, then $\varphi(A_1), \varphi(A_2), \dots, \varphi(A_Q)$ are independent random variables. That is,

$$\mathbb{P}\left(\bigcap_{i \in \mathcal{I}} \{\varphi(A_i) = z_i\}\right) = \prod_{i \in \mathcal{I}} \mathbb{P}(\varphi(A_i) = z_i), \quad z_i \in \mathbb{N} \cup \{0\}, \mathcal{I} \subseteq \{1, \dots, Q\}. \quad (15)$$

- (ii) The random variable $\varphi(A)$ follows a Poisson distribution, with expectation

$$\mathbb{E}[\varphi(A)] = \Lambda(A),$$

where $\Lambda(A)$ is known as the intensity measure. Let λ be the Radon-Nikodým derivative of Λ , so that $\Lambda(A) = \int_A \lambda(a) da$, then λ is known as the intensity function.

A log-Gaussian Cox process (LGCP) is a *doubly*-stochastic point process, where the intensity function λ of an inhomogeneous Poisson process is modelled as a stochastic process, or a random function, in itself. Specifically, the logarithm of the intensity is considered to follow a Gaussian process (GP) [25],

$$\log \lambda(\nu) \sim \text{GP}(\mathbf{0}, \Sigma(\nu, \nu'; \boldsymbol{\psi})), \quad (16)$$

where $\Sigma(\nu, \nu'; \boldsymbol{\psi})$ is the covariance function of the GP with parameter vector $\boldsymbol{\psi}$, evaluated at locations $\nu, \nu' \in \mathcal{S}$. We use a squared exponential covariance,

$$\Sigma(\nu, \nu'; \boldsymbol{\psi}) = \sigma_\lambda^2 \exp\left(-\frac{1}{2} \frac{(\nu - \nu')^2}{\ell^2}\right), \quad (17)$$

where σ_λ is the standard deviation of the GP and ℓ is its length scale parameter, so that $\boldsymbol{\psi} = (\sigma_\lambda, \ell)^T$.

The exact likelihood of the LGCP is intractable for continuous \mathcal{S} , so we follow the advice of [25] and discretize the domain. In our case, \mathcal{S} is already partitioned into disjoint subsets A_1, \dots, A_K at equally-spaced locations ν_1, \dots, ν_K , each being h wavenumbers apart, so that $\bigsqcup_{k=1}^K A_k = \mathcal{S}$ and $|\mathcal{S}| = Kh$. This is a result of the measurement technology, a spectrometer is capable of measurement at a discretized set of measurement points. This yields a natural, and unavoidable, discretization of the space \mathcal{S} with spacing h . In order to fit the LGCP, we need to translate the SMC samples for the line-narrowed spectrum $\mathbf{x}_{\text{LN},j}$ into approximate counts z_k of the number of Dirac delta functions located inside each subset A_k . However, these samples can have negative values due to the Gibbs phenomenon or ringing caused by the approximation of delta functions via Fourier transforms, as can be seen in Figure 2. Thus, we discretize and translate the samples so that a LGCP can be utilized. We initially marginalize the samples with respect to $\boldsymbol{\theta}$ and M as

$$\bar{x}_k := \mathbb{E}_{\boldsymbol{\theta}, M} [x_{\text{LN}}(\nu_k) \mid \mathbf{y}] \approx \frac{y_{\text{area}}}{J} \sum_{j=1}^J \frac{x_{\text{LN},j}(\nu_k; \boldsymbol{\theta}_j, M_j) \mathbb{1}_{x \geq 0}}{\sum_{k=1}^K x_{\text{LN},j}(\nu_k; \boldsymbol{\theta}_j, M_j) \mathbb{1}_{x \geq 0}}, \quad (18)$$

where \bar{x}_k denotes the posterior expectation for the line-narrowed spectrum at ν_k , $y_{\text{area}} = \sum_{k=1}^K y_k$ the area under the measurements, and $\mathbb{1}_{x \geq 0}$ is an indicator function

such that

$$\mathbb{1}_{x \geq 0} = \begin{cases} 1, & x_{\text{LN},j}(\nu_k; \boldsymbol{\theta}_j, M_j) \geq 0, \\ 0, & x_{\text{LN},j}(\nu_k; \boldsymbol{\theta}_j, M_j) < 0. \end{cases} \quad (19)$$

Next, we scale the values by a pre-defined constant of proportionality C and round the values to the closest integers. Given this, we obtain discretized and positive values $\mathbf{z} = (z_1, \dots, z_K)^T$ constructed as

$$z_k = \left\lfloor C\bar{x}_k + \frac{1}{2} \right\rfloor \quad (20)$$

where $\lfloor x \rfloor$ denotes the greatest integer $\leq x$.

Given the above, we are able to approximate the likelihood of the LGCP by

$$\mathcal{L}(\mathbf{z} \mid \mathbf{b}) = \prod_{k=1}^K \frac{\lambda(\nu_k)^{z_k}}{z_k!} \exp\{\lambda(\nu_k)\}, \quad (21)$$

where $\mathbf{b} = (\log \lambda(\nu_1), \dots, \log \lambda(\nu_K))^T$. In turn, the GP prior for \mathbf{b} can be evaluated as

$$\pi_0(\mathbf{b} \mid \boldsymbol{\psi}) = \frac{1}{\sqrt{(2\pi)^K}} |\Sigma(\boldsymbol{\nu}, \boldsymbol{\nu}; \boldsymbol{\psi})|^{-1/2} \exp\left\{-\frac{1}{2} \mathbf{b}^T \Sigma(\boldsymbol{\nu}, \boldsymbol{\nu}; \boldsymbol{\psi})^{-1} \mathbf{b}\right\}, \quad (22)$$

where $|\Sigma(\boldsymbol{\nu}, \boldsymbol{\nu}; \boldsymbol{\psi})|$ denotes the determinant of the $K \times K$ covariance matrix. The joint posterior distribution is then

$$\pi(\mathbf{b}, \boldsymbol{\psi} \mid \mathbf{z}) \propto \mathcal{L}(\mathbf{z} \mid \mathbf{b}) \pi_0(\mathbf{b} \mid \boldsymbol{\psi}) \pi_0(\boldsymbol{\psi}), \quad (23)$$

where $\pi_0(\boldsymbol{\psi})$ are priors for the parameters of the GP. For inference of the posterior defined in (23), we use MAP estimation via quasi-Newton optimization. Specifically, the limited-memory Broyden–Fletcher–Goldfarb–Shanno (L-BFGS) algorithm [20] as implemented in the GPstuff toolbox [35]. The discretized and positive values \mathbf{z} and corresponding MAP estimate for \mathbf{b} , along with 90% posterior credible intervals, are illustrated in the middle in Figure 2.

Finally, we construct a posterior distribution for the line shape locations \mathbf{l} by sampling the estimated GP. We use the local maxima of the sampled GP as our estimate for the peak locations \mathbf{l} . That is, where

$$\frac{\partial \log \lambda}{\partial \nu} = 0 \text{ and } \frac{\partial^2 \log \lambda}{\partial \nu^2} < 0. \quad (24)$$

Note that realizations of the GP must be at least twice differentiable in order for (24) to be valid. For example, the covariance function $\Sigma(\nu, \nu'; \boldsymbol{\psi})$ could be a Matérn with smoothness parameter $\zeta = 5/2$. Instead, we choose the squared exponential covariance (17), which is equivalent to a Matérn in the limit as $\zeta \rightarrow \infty$, since this is guaranteed to produce smooth realizations. We repeat the sampling for the GP local maxima 20000 times to construct a posterior distribution $\pi(\mathbf{l} \mid \mathbf{z})$. An example construction for this posterior is shown at the bottom of Figure 2.

5. Simulation-based Calibration. We use simulation-based calibration (SBC) [23, 34] to validate that our model is able to produce a consistent estimate of the number of peaks in the spectrum, N . Under mild assumptions, Bayesian posterior distributions have the property of self-consistency. This means that if we sample a parameter from its prior distribution,

$$\theta^* \sim \pi_0(\theta), \quad (25)$$

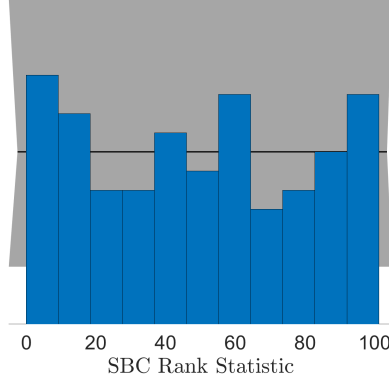


FIGURE 3. Simulation-based calibration histogram for the rank statistics of the true number of peaks N_s^* . The number of peaks were estimated as the number of local maxima in samples from the LGCP fits, using a GP length scale of 0.025. The histogram shows a uniform distribution. The solid black line shows the expected value and the shaded gray areas show the 99% confidence intervals.

and then simulate data from the generative model

$$\mathbf{y}^* \sim \mathcal{L}(\mathbf{y} \mid \theta^*), \quad (26)$$

then we expect that the resulting distribution $\pi(\theta \mid \mathbf{y}^*)$ of posterior probability should be concentrated in the vicinity of the true parameter value θ^* . This is particularly important in the context of our method, since we have replaced the true likelihood (8) with an approximation based on LOME, $\tilde{\mathcal{L}}(\mathbf{y} \mid \mathbf{x}_{\text{LN}}, \sigma_\epsilon^2)$ (10). We need to ensure that our approximation is accurate enough to still produce consistent estimates.

SBC involves generating multiple parameter values $\theta_1^*, \dots, \theta_S^*$ and corresponding synthetic datasets $\mathbf{y}_1^*, \dots, \mathbf{y}_S^*$ from their joint distribution,

$$(\mathbf{y}_s^*, \theta_s^*) \sim \pi(\mathbf{y}, \theta), \quad (27)$$

where $\pi(\mathbf{y}, \theta) = \mathcal{L}(\mathbf{y} \mid \theta) \pi_0(\theta)$. For our model, we first simulate a realization of a GP, \mathbf{b}_s^* . We can then determine the peak locations \mathbf{l}_s^* and number of peaks N_s^* from the maxima of this function, as previously explained in Section 4. Next, we simulate amplitudes \mathbf{a}_s^* and line shape parameter γ_s^* for the peaks. We can then evaluate $f(\nu; \delta_N(\nu; \mathbf{a}_s^*, \mathbf{l}_s^*), \theta_s^*)$ at wavenumbers ν_1, \dots, ν_K and add white noise to produce synthetic data \mathbf{y}_s^* according to (1). In our case, we produce $S = 100$ pairs of parameters and datasets from the joint distribution. The prior distributions for the parameters are described in Section 6.

We run Algorithm 1 to obtain samples from the approximate posterior for \mathbf{x}_{LN} given \mathbf{y}_s^* , then use L-BFGS to fit the LGCP. Finally, we repeatedly sample $\mathbf{b}_s^{(j)}$ from the GP for $j = 1, \dots, J$ and find the maxima of each function to obtain posterior samples $\mathbf{l}_s^{(j)}$ and $N_s^{(j)}$. We use $J=20000$ posterior samples as described in Section 4. Under Bayesian self-consistency, the rank r_s of the true parameter N_s^* should be

TABLE 1. Prior distributions for the Lorentz and Voigt line shape parameters $\boldsymbol{\theta}$, the Fourier self-deconvolution cut-off parameter M , and the GP covariance parameters ψ .

Prior	Lorentz	Voigt
$\pi_0(\gamma)$	$\mathcal{U}(1, 30)$	$\mathcal{U}(1, 30)$
$\pi_0(\sigma \mid \gamma)$	NA	$\mathcal{N}_+(0.5 \times \gamma, (0.05 \times \gamma)^2)$
$\pi_0(M)$	$\mathcal{U}(10, 80)$	$\mathcal{U}(10, 80)$
$\pi_0(\log\{\sigma_\lambda\})$	$t(0, 100^2, 10)$	$t(0.01, 100^2, 10)$

uniformly-distributed under the corresponding posterior,

$$\begin{aligned}
 r_s &= \text{rank} \left[N_s^*, (N_s^{(1)}, \dots, N_s^{(J)}) \right] \\
 &= \sum_{j=1}^J \mathbb{1} \left[N_s^{(j)} < N_s^* \right]
 \end{aligned} \tag{28}$$

where $\mathbb{1}[x]$ is the indicator function, therefore r_s is a number between 0 and J . Figure 3 shows that these ranks r_1, \dots, r_S are indeed uniformly-distributed, as required by SBC.

6. Prior Distributions and Computational Details. We use a continuous uniform distribution for the line width parameter γ for both Lorentz and Voigt profiles, with σ modelled as a truncated normal distribution conditional on γ . A discrete uniform distribution is used for the cut-off parameter M . We use a fixed value for the length scale parameter ℓ of the GP covariance function. The prior for the GP covariance parameter σ_λ is specified on a logarithmic scale. We use Student's t distributions $t(\mu, \delta^2, \nu_{\text{Fr}})$ parameterized according to mean, variance, and degrees of freedom. We detail these prior distributions in Table 1. More specifically we set $\pi_0(\gamma) = \mathcal{U}(1, 30)$ and $\pi_0(M) = \mathcal{U}(10, 80)$, meaning that the half-width at half-maximum (HWHM) of the peaks is limited to a range between 1 cm^{-1} and 30 cm^{-1} and the number of Fourier self-deconvolution points is limited to lay in the interval $[10, 80]$. This prior on M has an important effect in regularizing the discrete Fourier approximation given by Equation (9). If M is too large, then the posterior for \mathbf{x}_{LN} will be dominated by ringing artifacts and boundary effects, making it impossible to determine the peak locations. The theoretical maximum number of peaks that can be represented by $g(\nu_k, \boldsymbol{\theta}, M)$ is $0.5M$ [17]. In practice, we recommend setting the upper bound for $\pi_0(M)$ to be at least four times the maximum number of peaks in the spectrum, but small enough that the effect of ringing artifacts is minimized.

The SMC was run with $J = 1000$ particles with residual resampling initiated when ESS falls below a threshold of $J_{\min} = J/2$. We use a Metropolis-Hastings random walk kernel for the MCMC updates. The MCMC proposals for new particles $(\gamma, M)_{1:J}^*$ are constructed as

$$\begin{aligned}
 (\boldsymbol{\theta}_j^*, \widetilde{M}_j^*) &= (\boldsymbol{\theta}_j, M_j) + \zeta, \\
 M_j^* &= \left\lfloor \widetilde{M} + \frac{1}{2} \right\rfloor + \zeta_M,
 \end{aligned} \tag{29}$$

where $\zeta \sim \mathcal{N}(0, c\Sigma_{\boldsymbol{\theta}, N})$ with $\Sigma_{\boldsymbol{\theta}, N}$ denoting an empirical covariance of the current particles $(\boldsymbol{\theta}, N)_{1:J}$, scaled according to $c \in R_+$ such that the acceptance rate is

approximately a pre-defined target acceptance rate, and with a discrete random walk $\zeta_M \sim \mathcal{U}(-1, 1)$. New particles $\mathbf{x}_{\text{LP},j}(\boldsymbol{\nu}, \boldsymbol{\theta}_j^*, M_j^*)$ are then be computed according to the linear prediction method. The target acceptance rate was set to 0.30 with 5 MCMC updates during each iteration step. There exist methods of automatically determining the number of MCMC updates at each iteration step, see for example [5] and references therein.

7. Results. In addition to the SBC study described in Section 5, we have also applied our SMC-sampled LOMEP algorithm to 4 other synthetic spectra, as well as a mineralogical Raman spectrum and two coherent anti-Stokes Raman spectra (CARS) of proteins. All of the syntethic spectra were constructed using noise variance $\sigma_\epsilon^2 = 0.025^2$. The results for the 4 synthetic spectra and the 2 proteins are available in the online supplementary material.

The posterior distributions for the peak locations for a synthetic spectrum used in the SBC study are shown in Figure 4. We can see here that the true peak locations \mathbf{l} are contained within the posterior distribution $\pi(\mathbf{l} \mid \mathbf{z})$ constructed with the sampled local maxima of the LGCP. Figure 4 also shows the posterior distributions for the Lorentz line width parameter γ along with the posterior for the number of peaks N . Both posteriors contain the true parameter values used to generate the spectrum. We also calculated the average bias of -0.1 for the posterior mean estimates of the number of peaks N , as well as root-mean square error (RMSE) of 1.52 and coverage of 0.97 for the 95% posterior credible intervals in the SBC study.

We analyze a Raman spectrum of anorthite ($\text{Ca Al}_2 \text{ Si}_2 \text{ O}_8$), a type of feldspar, which was obtained from the RRUFF database [18, ID: R040059]. This sample is from the collection of the University of Arizona Mineral Museum. We use the same prior distributions for all of the experimental data as for the synthetic spectra, detailed in Table 1. The posterior distributions for the line-shape parameter γ and number of line shapes N are shown in Figure 5. The 25 known peak locations for anorthite are given in Table 4 of [10, p. 1488]. These locations are illustrated with black dots in Figure 5, along with the estimated posterior distributions $\pi(\mathbf{l} \mid \mathbf{z})$. Our method has detected some additional peak locations which appear reasonable, including one near 600cm^{-1} that corresponds with a clear hump in the data, but which seems to have been previously unknown.

8. Conclusions. We present a Bayesian model for line narrowing of spectroscopic data that is applicable for any parameterizable kernel function. In this paper, we particularly focus on Lorentzian and Voigt line shapes, which are typical of electromagnetic spectra. The key innovation of our method is the use of a log-Gaussian Cox process to provide an interpretable posterior for the line narrowing and correct for unwanted peak splitting effects due to Fourier self-deconvolution. This addresses the major limitations of the LOMEP algorithm for line narrowing [14, 15].

In many real-world applications, the true peak locations are unknown *a priori*, which limits the application of existing methods such as [24, 27]. Our proposed method provides posterior distributions for the peak locations, along with the line-shape parameters. These can then be used as input for further chemometric analysis. We have validated our proposed method using synthetic data sets and simulation-based calibration, demonstrating that the smoothed LGCP posterior is able to recover the true peak locations. We also applied our method to three experimental Raman spectra, one of which that exhibited a low signal-to-noise ratio. In all three

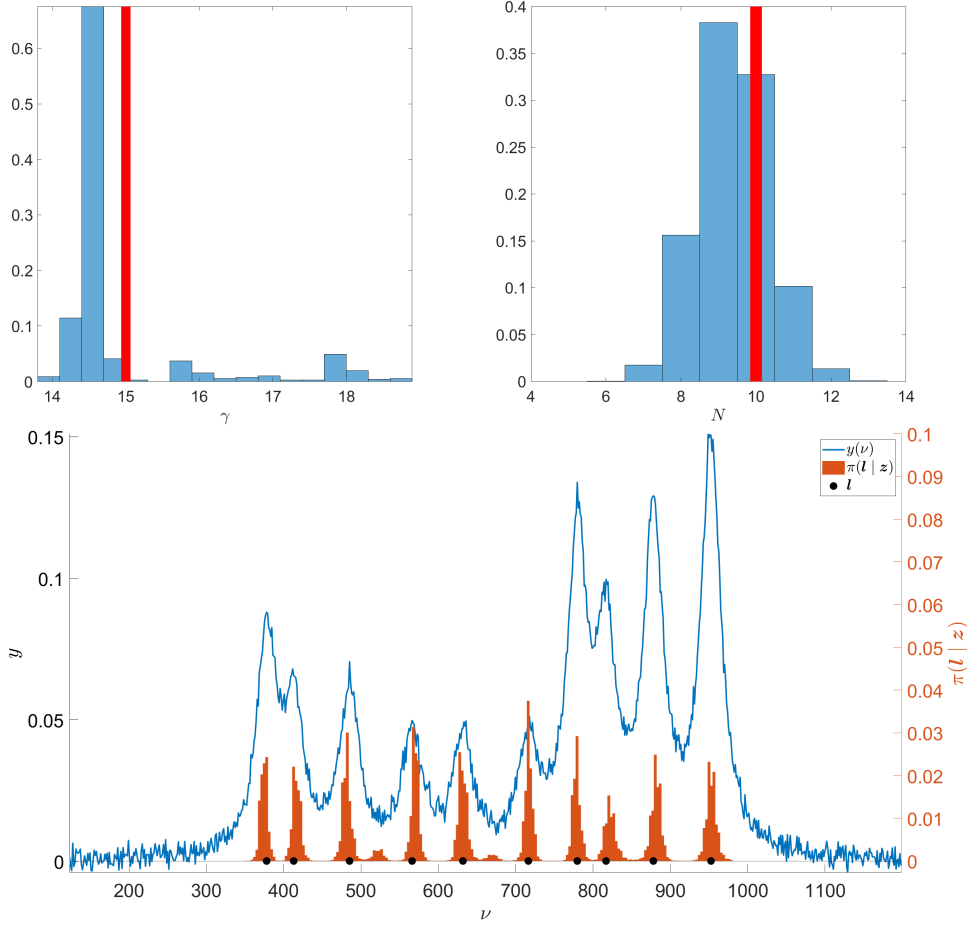


FIGURE 4. At the top, posterior distributions for the line shape parameter γ and the number of line shapes N along with their respective true parameter values used to generate the synthetic spectrum in red. At the bottom, the corresponding synthetic spectrum (in blue) and the corresponding location posterior $\pi(\mathbf{l} | \mathbf{z})$ (in red). Black dots denote the locations used to generate the spectrum.

cases, were able to obtain an interpretable posterior for the peak locations that corresponded well with the known spectroscopic properties of the particular mineral sample and the protein samples. This is in contrast to many existing methods, such as [11, 12], that only work well in low-noise environments, or with a small number of peaks.

Although we have focused mainly on Raman spectroscopy here, our method is much more broadly applicable. It has the potential to be used for practically any spectroscopic measurement of electromagnetic phenomena, from X-rays [33] to radar [36]. By substituting the Lorentzian or Voigt line shapes with a suitable alternative, it could be applied to any time series where the periodogram can be represented as a convex combination of known spectral density functions, such as measurements of ocean waves [32]. Depending on the application, a different choice of point process

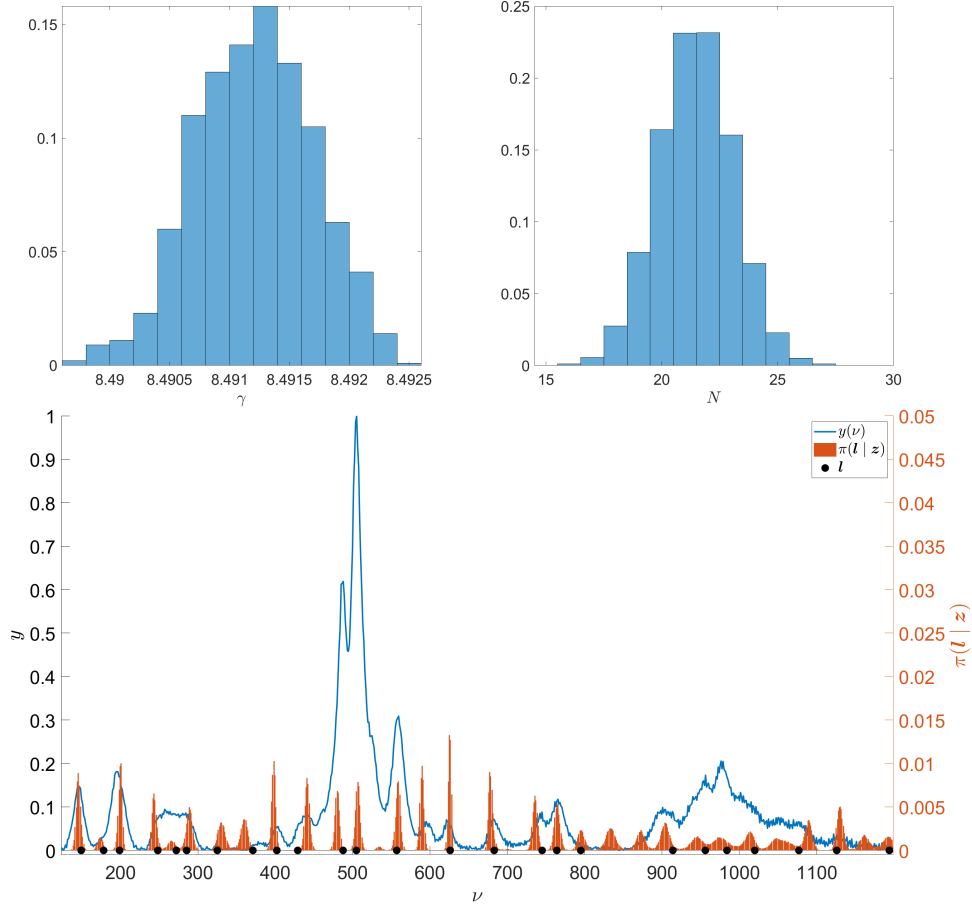


FIGURE 5. At the top, posterior distributions for the line shape parameter γ and the number of line shapes N . At the bottom, the observed Raman spectrum of anorthite (in blue) and the corresponding location posterior $\pi(l | z)$ (in red). Black dots denote the peak locations found in literature [10].

model might also be needed. For example, peak locations in mass spectrometry might be better modelled as a self-exciting point process, such as a Hawkes process [26].

Acknowledgments. This work has been funded by the Academy of Finland (project numbers 327734, 334816, and 336787). The authors thank Andreas Rupp for helpful conversations during the preparation of this manuscript. We also thank the associate editor and two reviewers for their thoughtful comments and suggestions.

REFERENCES

- [1] P. J. Brockwell and R. A. Davis, *Introduction to Time Series and Forecasting*, Springer, 2016.
- [2] B. Buttingsrud and B. K. Alsberg, A new maximum entropy-based method for deconvolution of spectra with heteroscedastic noise, *Journal of Chemometrics*, **18** (2004), 537–547.
- [3] N. Chopin and O. Papaspiliopoulos, *An Introduction to Sequential Monte Carlo*, Springer Series in Statistics, Springer, 2020.
- [4] H. Cui, G. Xia, S. Jin, L. Cheng, L. Bai, L. Ma and Y. Fang, Levenberg–Marquardt algorithm with adaptive Tikhonov regularization for bandwidth correction of spectra, *Journal of Modern Optics*, **67** (2020), 661–670.
- [5] H.-D. Dau and N. Chopin, Waste-free sequential Monte Carlo, *Journal of the Royal Statistical Society: Series B (Statistical Methodology)*, **84** (2022), 114–148.
- [6] P. Del Moral, A. Doucet and A. Jasra, Sequential Monte Carlo samplers, *Journal of the Royal Statistical Society: Series B*, **68** (2006), 411–436.
- [7] P. Del Moral, A. Doucet and A. Jasra, An adaptive sequential Monte Carlo method for approximate Bayesian computation, *Statistics and Computing*, **22** (2012), 1009–1020.
- [8] M. Diem, *Modern Vibrational Spectroscopy and Micro-Spectroscopy: Theory, Instrumentation and Biomedical Applications*, John Wiley & Sons, 2015.
- [9] P. J. Diggle, P. Moraga, B. Rowlingson and B. M. Taylor, Spatial and spatio-temporal log-Gaussian Cox processes: Extending the geostatistical paradigm, *Statistical Science*, **28** (2013), 542 – 563.
- [10] J. J. Freeman, A. Wang, K. E. Kuebler, B. L. Jolliff and L. A. Haskin, Characterization of natural feldspars by Raman spectroscopy for future planetary exploration, *The Canadian Mineralogist*, **46** (2008), 1477–1500.
- [11] K. B. Frøhling, T. S. Alstrøm, M. Bache, M. S. Schmidt, M. N. Schmidt, J. Larsen, M. H. Jakobsen and A. Boisen, Surface-enhanced Raman spectroscopic study of DNA and 6-mercapto-1-hexanol interactions using large area mapping, *Vibrational Spectroscopy*, **86** (2016), 331–336.
- [12] S. Gulam Razul, W. Fitzgerald and C. Andrieu, Bayesian model selection and parameter estimation of nuclear emission spectra using RJMCMC, *Nuclear Instruments and Methods in Physics Research Section A: Accelerators, Spectrometers, Detectors and Associated Equipment*, **497** (2003), 492–510.
- [13] T. Härkönen, L. Roininen, M. T. Moores and E. M. Vartiainen, Bayesian quantification for coherent anti-Stokes Raman scattering spectroscopy, *The Journal of Physical Chemistry B*, **124** (2020), 7005–7012.
- [14] J. K. Kauppinen, D. J. Moffatt, M. R. Hollberg and H. H. Mantsch, A new line-narrowing procedure based on Fourier self-deconvolution, maximum entropy, and linear prediction, *Applied Spectroscopy*, **45** (1991), 411–416.
- [15] J. K. Kauppinen, D. J. Moffatt and H. H. Mantsch, Nonlinearity of the maximum entropy method in resolution enhancement, *Canadian Journal of Chemistry*, **70** (1992), 2887–2894.
- [16] J. K. Kauppinen, D. J. Moffatt, H. H. Mantsch and D. G. Cameron, Fourier self-deconvolution: A method for resolving intrinsically overlapped bands, *Applied Spectroscopy*, **35** (1981), 271–276.
- [17] J. K. Kauppinen and J. Partanen, *Fourier Transforms in Spectroscopy*, Wiley, Berlin, 2001.
- [18] B. Lafuente, R. T. Downs, H. Yang, and N. Stone, The power of databases: the RRUFF project, in *Highlights in Mineralogical Crystallography* (eds. T. Armbruster and R. M. Danisi), W. De Gruyter, 2015, 1–30.
- [19] G. Last and M. D. Penrose, *Lectures on the Poisson Process*, Cambridge University Press, 2017.
- [20] D. C. Liu and J. Nocedal, On the limited memory BFGS method for large scale optimization, *Mathematical Programming*, **45** (1989), 503–528.
- [21] H. Liu, L. Yan, Y. Chang, H. Fang and T. Zhang, Spectral deconvolution and feature extraction with robust adaptive Tikhonov regularization, *IEEE Transactions on Instrumentation and Measurement*, **62** (2013), 315–327.
- [22] V. A. Lórenz-Fonfría and E. Padrós, Maximum entropy deconvolution of infrared spectra: Use of a novel entropy expression without sign restriction, *Applied Spectroscopy*, **59** (2005), 474–486.

- [23] J. McLeod and F. Simpson, Validating Gaussian process models with simulation-based calibration, in *2021 IEEE International Conference on Artificial Intelligence Testing (AITest)*, 2021, 101–102.
- [24] M. T. Moores, K. Gracie, J. Carson, K. Faulds, D. Graham and M. Girolami, Bayesian modelling and quantification of Raman spectroscopy, 2016, arXiv preprint 1604.07299.
- [25] J. Møller, A. R. Syversveen and R. P. Waagepetersen, Log Gaussian Cox processes, *Scandinavian Journal of Statistics*, **25** (1998), 451–482.
- [26] J. G. Rasmussen, Bayesian inference for Hawkes processes, *Methodology and Computing in Applied Probability*, **15** (2011), 623–642.
- [27] C. Ritter, Statistical analysis of spectra from electron spectroscopy for chemical analysis, *The Statistician*, **43** (1994), 111–127.
- [28] S. Särkkä, *Bayesian Filtering and Smoothing*, Cambridge University Press, 2013.
- [29] L. Serra, M. Saez, J. Mateu, D. Varga, P. Juan, C. Díaz-Ávalos and H. Rue, Spatio-temporal log-Gaussian Cox processes for modelling wildfire occurrence: the case of Catalonia, 1994–2008, *Environmental and Ecological Statistics*, **21** (2014), 531–563.
- [30] S. Shirota and A. E. Gelfand, Space and circular time log Gaussian Cox processes with application to crime event data, *The Annals of Applied Statistics*, **11** (2017), 481 – 503.
- [31] E. Smith and G. Dent, *Modern Raman Spectroscopy: A Practical Approach*, 2nd edition, John Wiley & Sons, 2019.
- [32] R. H. Stewart, *Introduction to Physical Oceanography*, Texas A&M University, 2004.
- [33] J. Suuronen, M. Emzir, S. Lasanen, S. Särkkä and L. Roininen, Enhancing industrial X-ray tomography by data-centric statistical methods, *Data-Centric Engineering*, **1** (2020), e10.
- [34] S. Talts, M. Betancourt, D. Simpson, A. Vehtari and A. Gelman, Validating Bayesian inference algorithms with simulation-based calibration, 2020, arXiv preprint 1804.06788.
- [35] J. Vanhatalo, J. Riihimäki, J. Hartikainen, P. Jylänki, V. Tolvanen and A. Vehtari, GPstuff: Bayesian modeling with Gaussian processes, *Journal of Machine Learning Research*, **14** (2013), 1175–1179.
- [36] I. I. Virtanen, H. W. Tesfaw, L. Roininen, S. Lasanen and A. Aikio, Bayesian filtering in incoherent scatter plasma parameter fits, *Journal of Geophysical Research: Space Physics*, **126** (2021), e2020JA028700.
- [37] P. Whittle, Estimation and information in stationary time series, *Arkiv för Matematik*, **2** (1953), 423–434.

Received xxxx 20xx; revised xxxx 20xx.

E-mail address: teemu.harkonen@lut.fi

E-mail address: emma.hannula@student.lut.fi

E-mail address: mmoores@uow.edu.au

E-mail address: erik.vartiainen@lut.fi

E-mail address: lassi.roininen@lut.fi